International Journal of Mass Spectrometry 307 (2011) 39–45

Contents lists available at ScienceDirect

International Journal of Mass Spectrometry

journal homepage: www.elsevier.com/locate/ijms

High spatial resolution trace element analysis by LA-ICP-MS using a novel ablation cell for multiple or large samples

Mattias B. Fricker[a], Daniel Kutscher[b], Beat Aeschlimann[a], Jakob Frommer[a], Rolf Dietiker[a], Jörg Bettmer[b], Detlef Günther[a,*]

[a] ETH Zurich, Laboratory of Inorganic Chemistry, Wolfgang-Pauli-Strasse 10, 8093 Zurich, Switzerland
[b] University of Oviedo, Department for Physical- and Analytical Chemistry, Julian Clavería 8, 33006 Oviedo, Spain

ARTICLE INFO

Article history:
Received 24 November 2010
Received in revised form 10 January 2011
Accepted 11 January 2011
Available online 15 January 2011

Keywords:
LA-ICP-MS
Ablation cell
Large sample
Fast washout
Gel electrophoresis
CFD modeling

ABSTRACT

An ablation cell was developed to host large or several small samples (up to dimensions 230 mm × 34 mm × 16 mm, $L \times W \times D$) for high spatial resolution analysis. The performance of the cell was tested using silicate glass NIST SRM 610 and steel CRM JK-2D. To obtain high resolution profiles of trace element distributions, the ablation cell must offer fast washout of the aerosol to decrease mixing of the particles from different laser pulses. The washout of the new ablation cell is 70% faster when compared to the standard ablation cell previously applied in our laboratory and provides washout times within 2.6 s for 99.9% of the signal. Gas flow patterns in the cell were modeled by computational fluid dynamics (CFD) and validated by measurements on two reference materials. To demonstrate the potential of the ablation cell, p-(hydroxymercuri)benzoic acid (pHMB) derivatised ovalbumin was ablated from polyacrylamide gels after electrophoretic separation.

The evaluation of the ablation cell demonstrates high resolution capabilities on large solid samples. It promises to have a significant impact on numerous applications, such as imaging of biological samples or trace element determinations on climate archives (e.g., stalagmites).

1. Introduction

Laser ablation-inductively coupled plasma-mass spectrometry (LA-ICP-MS) is a widespread technique for analysis of major, minor and trace elements in solid samples with high dynamic range and low limits of detection [1]. Quantitative analysis of elements and isotopes are required in a wide variety of applications (bulk analysis, micro analysis, fingerprinting [2], depth profiling [3], line scans [4–8], isotope ratio analysis [9], and mapping [10–12] in many research fields [13] (earth sciences, forensics, gemology, material sciences, life sciences and in industry). In recent years, the detection of metal containing proteins after separation on polyacrylamide gels has become a frequent application for LA-ICP-MS [14]. Especially electrophoresis in two dimensions provides high separation efficiency for a given sample. However, sensitive and spatially resolved detection is a prerequisite for the successful interpretation [15] of these gels.

The performance of LA-ICP-MS is crucially dependent on the characteristics of the ablation cell. Various investigations on ablation cell design have been carried out on the volume of the cell and transport tube material [9,16], transport efficiency in dependence on geometry [17–19], as well as on the applicability of cooled cells for hosting tissues [20], open-contact cell for large, flat samples [21] or double cell configurations with fast washout [22]. However, so far the different designs have not led to the development of an ablation cell, which can host large samples enclosed in an airtight Argon or Helium atmosphere. Since fast washout requires a small volume, a number of small cell volumes or double cells have been reported in the literature. Fast washout and transport of the laser generated aerosol to the ICP have been extensively studied for different ablation cell designs and approaches such as a laminar flow cell [23], cell in a cell [17,18,22,24], using the venturi effect [25], rotating nozzle [26], cyclonic gas flow [27], and removing the cell by in-torch ablation [28]. Numeric modeling of gas flows [29,30] and particle trajectories [19] in the ablation cell are becoming a valuable source of information for designing and optimizing of new ablation cells for specialized purposes. Some of these small volume cells would be ideal to be placed on large sample holders. However, as indicated by Lindner et al. [31], this requires the design of a specific interface.

The requirement of large ablation cells evolved from a number of applications, where the samples cannot be cut into pieces for analysis, such as historic artifacts, precious objects, corals or stalagmites. For the tightly grown stalagmites, a cutting process

* Corresponding author at: ETH Zurich, Laboratory of Inorganic Chemistry, HCI G113, Wolfgang-Pauli-Strasse 10, 8093 Zurich, Switzerland. Tel.: +41 44 632 4687; fax: +41 44 633 1071.
E-mail address: guenther@inorg.chem.ethz.ch (D. Günther).

1387-3806/$ – see front matter © 2011 Elsevier B.V. All rights reserved.
doi:10.1016/j.ijms.2011.01.008

would lead to significant loss of information recorded in the sample. For bulk analysis, a short washout of the aerosol is not critical. However, it is essential for analysis with high spatial resolution for scanning and mapping of solid sample surfaces. While in scanning mode, laser ablation runs along a heterogeneous sample (such as sediments [32], corals [5], stalagmites [10,33], biological tissue [11,34], etc.) the composition of the aerosols changes over time and therefore needs to be recorded as a transient signal without mixing of information [3,35,36].

Based on the literature and the variety of samples analyzed in our laboratory, we focused on the development of a routinely applicable ablation cell design for high resolution analyses of large, heterogeneous samples. The parameters of interest included signal intensities (transport efficiency) and stability in dependence of the position of ablation. These studies were carried out using prolonged ablation of profiles across two standard materials. The empirical investigations were furthermore validated by gas flow velocity simulations using computational fluid dynamics (CFD). Finally, we applied the ablation cell to perform imaging of the distribution of a pHMB-derivatised protein after electrophoretic separation using the intensity profile of mercury. As natural ovalbumin contains only S and P (but no metals) for detection with Q-ICP-MS, the artificial introduction of Hg was necessary to improve detection capabilities.

2. Experimental

2.1. Instrumentation

All analyses were carried out using an ArF excimer laser at 193 nm (GeoLasC, Lambda Physik, Göttingen, Germany), the ablation cell was mounted on a computer-controlled xyz-stage of an Olympus BX51 microscope. The prototype ablation cell was built in-house to host samples with max. dimensions of 230 mm × 34 mm × 16 mm ($L \times W \times D$). The total volume of the cell is around 1 L, whereas the volume, into which the laser aerosol expansion takes place, is only around 13 cm^3. The entire corpus was made from polymethylmethacrylate (PMMA) to provide a small weight (2.2 kg) of the ablation cell, see Fig. 1. The ablation cell was coupled to a quadrupole ICP-MS (ELAN DRC$^+$, Perkin Elmer, Massachusetts, USA, or Agilent 7500cs, Agilent Technologies, Palo Alto, USA). The ICP-MS were tuned daily for high signal intensity and $ThO^+/Th^+ < 1.5\%$, and operating conditions of the laser and the ICP-MS are summarized in Table 1. A standard cylindrical ablation cell (volume of 63 cm^3, for samples up to 50 mm diameter) used in our labs [37] was used to compare washouts.

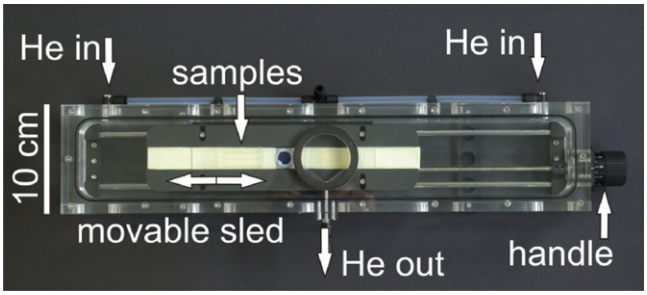

Fig. 1. Top view of the ablation cell. During analysis the entire cell is moved by a computer-controlled xyz-stage for LA scanning through the round window in the center. The sample is fixed on a sled within the cell, allowing manual repositioning between analyses without opening of the cell. With the 50 mm diameter cell window, it is possible to scan about 40 mm on the sample before moving the sled manually with the handle. The dimensions of the chamber housing the sled are 450 mm × 70 mm × 40 mm L × W × D. On this photograph, two halves of a polyacrylamide gel (not stained) and one NIST SRM 610 are mounted on the sled, one ready for ablation in front of the He outlet.

2.2. Modeling

To validate the assumptions about the gas flow patterns within the ablation cell, the gas flow dynamics were modeled with Ansys CFX 11.0 [38] using an optimized fine numerical grid of about 1.8 million elements. The fluid was set to Helium at standard temperature and pressure (STP). The boundary conditions, i.e., inflow and outflow were based on experimental data and set to a mass flow of 2.9767×10^{-3} g s^{-1} at 25 °C (1 L min^{-1}).

2.3. Characterization

The design allows fitting large samples without further cutting. For testing the performance of the cell, NIST 610 SRM was placed in a PMMA slab (Fig. 2) mimicking the contour of a cuboid sample. Based on this, it was assured that gas flow conditions on the sample surface are close to those from modeling. The ablation experiments were carried out on three NIST 610 glasses, which were placed into the sample holder underneath the ablation cell window, as illustrated in Fig. 3. Scans were performed three times along the axis in the center of each sample. They were repeated for 3 positions of the sled, at the end of the cell away from the He inlet (position q), in the center (position o) and at the He inlet (position p), respectively. All observations for signal intensity, stability and washout are based on multielement measurements. The signal of $^{23}Na^+$ was selected as

Table 1
Operating conditions of both the excimer laser and the quadrupole ICP-MS and list of isotopes (m/Z) that were monitored for analyses of NIST 610, JK-2D and the electrophoresis gels.

	NIST 610 cleaning	NIST 610 acquisition	JK-2D	Gel
Laser ablation				
Scan length (mm)	5.5	5.5	28.6	35.7
Energy density (J cm^{-2})	6.5	6.5	26	14
Crater size (μm)	127	63	90	160
Repetition rate (Hz)	1	10	10	20
Scanning speed (μm s^{-1})	47	20	90	50
ICP-MS				
Instrument	ELAN DRC+		ELAN DRC+	Agilent
RF power (W)	1400		1380	1600
Carrier gas, He (L min^{-1})	1.0		1.0	1.0
Nebulizer gas, Ar (L min^{-1})	0.95		0.86	0.75
Aux. gas, Ar (L min^{-1})	0.84		0.75	
Plasma gas, Ar (L min^{-1})	17.0		17.5	15.0
Dwell time (ms)	10		10	50
Sweep time (ms)	650		208	312

NIST 610: 7Li, 11B, 13C, 23Na, 24Mg, 25Mg, 26Mg, 27Al, 29Si, 31P, 34S, 35Cl, 39K, 42Ca, 43Ca, 46Ca, 49Ti, 53Cr, 55Mn, 57Fe, 59Co, 60Ni, 65Cu, 66Zn, 71Ga, 79Br, 85Rb, 88Sr, 89Y, 133Cs, 137Ba, 139La, 140Ce, 141Pr, 146Nd, 147Sm, 153Eu, 157Gd, 159Tb, 163Dy, 165Ho, 166Er, 169Tm, 173Yb, 175Lu, 178Hf, 181Ta, 208Pb, 232Th, 238U; JK-2D: 13C, 23Na, 27Al, 29Si, 31P, 32S, 34S, 53Cr, 55Mn, 57Fe, 59Co, 60Ni, 63Cu, 95Mo, 118Sn, 208Pb; Gel: 13C, 29Si, 34S, 199Hg, 200Hg, 202Hg.

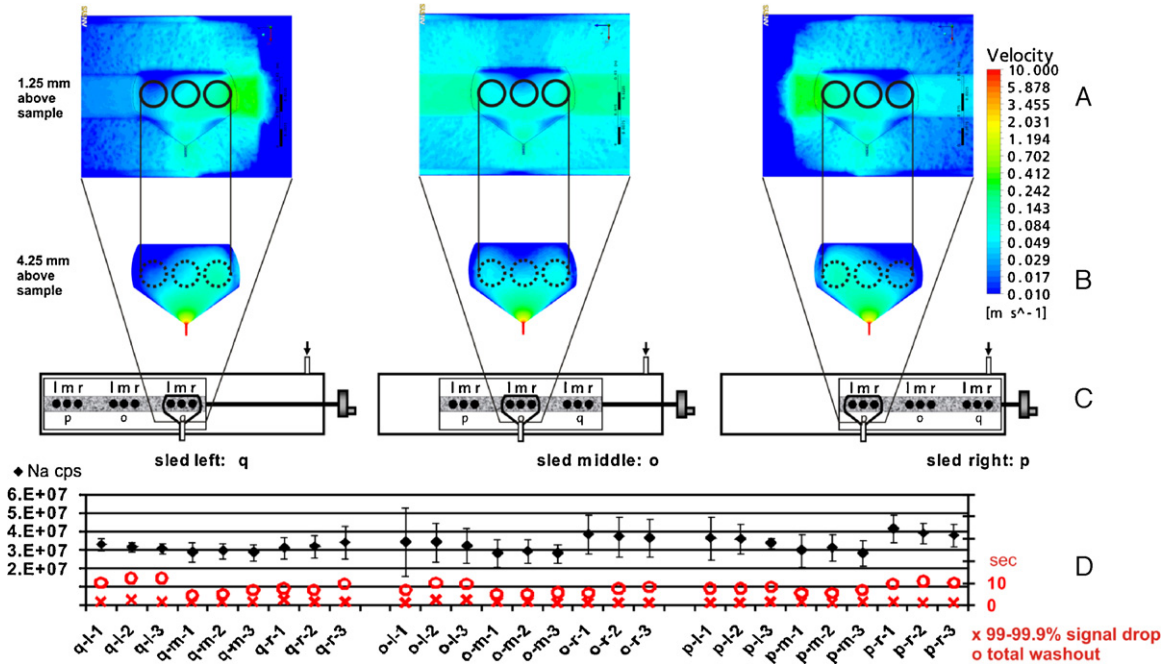

Fig. 2. Gas flow models showing gas velocities (m s^{-1}) at the ablation area, 1.25 mm above the surface of the sample (A) and insets (B) displaying gas velocity at the level of the outlet, 4.25 mm. Sketches (C) of the cell indicate the position of the sled and the samples (NIST 610) respectively. Signal intensity [cps] of Na (diamonds) is given in plot (D), three repetitions for each sample at each position (1–3). Aerosol washout time is shown in the same plot (D) for the complete washout (circles), i.e., drop of the signal to background level and for the fast washout (crosses), i.e., drop of the signal of 2–3 order of magnitudes (99–99.9% signal drop).

a representative for cell evaluation, since Na is monoisotopic with a high concentration in NIST 610. This element provides high signal intensity and is thus very suitable for the determination of the washout time. The steel sample JK-2D was placed in the center of the sled and embedded in the same way as the three NIST 610 samples. Line scans of 28.6 mm length (scan 1 and 2 were shorter, due to geometry) were performed 12 times with a distance of 2.5 mm between the scans, see Fig. 4. Each line was scanned twice: the first time for cleaning of the sample surface and the second time for the data acquisition. The steel sample analysis was carried out using two gas inlets enabling more symmetric gas flows and reducing purging time after closing of the cell when samples were mounted. Furthermore, for the measurements on the steel sample and the gel, the volume at the ablation area was increased to a near circular shape (Fig. 4B) in order to suppress the low flow zones as observed in the simulations (Fig. 3).

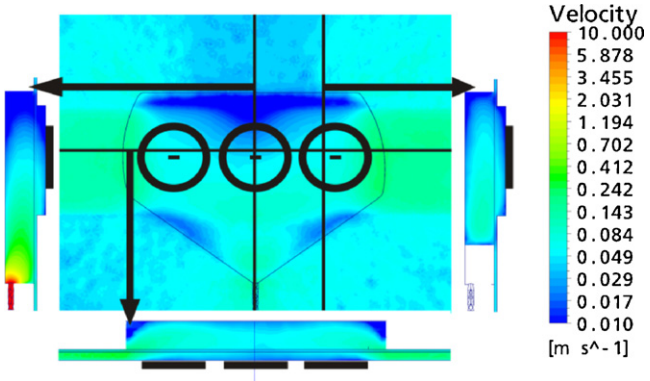

Fig. 3. Gas flow velocities (m s^{-1}) modeled using Ansys. The black circles indicate the location of the three NIST SRM 610. A horizontal and two vertical cross-sections are shown on the sides. The cross-section through the center of the gas outlet (vertical on the left) shows the slightly larger low gas flow area (dark blue) compared to the cross-section on the side (vertical on the right). (For interpretation of the references to color in the text, the reader is referred to the web version of the article.)

2.4. Application

Derivatisation of ovalbumin with p-(hydroxymercuri)benzoic acid (pHMB) was carried out as described elsewhere [39]. Ovalbumin (Sigma Aldrich) was dissolved in 50 mmol L^{-1} NH_4HCO_3 (Sigma Aldrich) in ultrapure water (Millipore, Bedford, USA) to the desired concentration and then incubated with a 10-fold molar excess of pHMB (25 μmol L^{-1} in 0.05 mol L^{-1} NaOH) per cysteine residue. After two-fold ultrafiltration using a 10 kDa cutoff membrane (Millipore, Bedford, USA), the derivatised protein was diluted with 50 mmol L^{-1} NH_4HCO_3. After incubation in the sample buffer (62.5 mmol L^{-1} Tris, pH 6.8, 2% SDS, 25% glycerol, 0.01% bromophenol blue), 1 μL of this solution was loaded on the gel. Gel electrophoresis was carried out using precast gels (PhastGel 12.5% separation gel, dimensions 43 mm × 50 mm × 0.45 mm, GE Healthcare) on a PhastGel electrophoresis unit (GE Healthcare) for 30 min at 250 V. Following the procedure described by Raab et al. [8], the gels were shaken in glycerol for 2 min, to exchange remaining water before drying at 70 °C for 2 h. The exchange of water to glycerol was necessary to avoid deformation or breaking of the gel during drying. For laser ablation, the gels were divided in two pieces along the middle of the chromatographic axis, fixed onto a glass slide with double sided tape and mounted into the ablation cell together with a NIST SRM 610 for tuning of the instrument. For comparison, one gel was stained using Coomassie Blue.

3. Results and discussion

3.1. Modeling

Modeling of the gas flow velocities in the cell suggested non-symmetric gas velocities in the ablation area, when ablating at different positions of samples and sample holder. Symmetric gas flows – which are favorable for analysis – were observed only in the center position of the sled. All measurements on NIST 610 were performed using a single gas inlet in one corner of the cell (Fig. 2C).

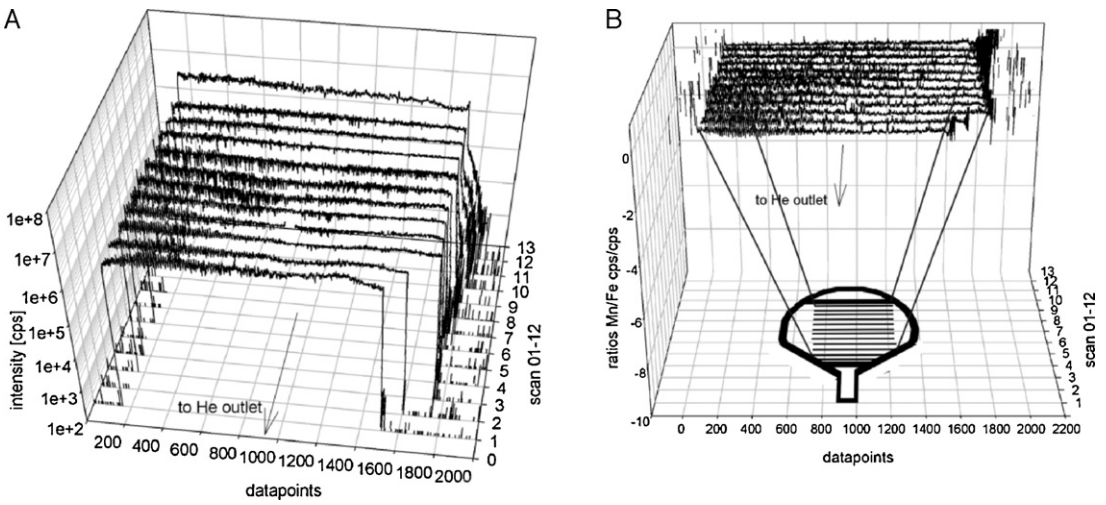

Fig. 4. (A) Signal intensity map on JK-2D shown for $^{57}Fe^{+}$, scan 01 closest to the edge at the outlet, scan 12 closest to the far edge, both with unstable (wavy) signals. The left half of all line scans is noisier than the right half and washout is longer for the scans further away from the outlet. Missing data (middle of the line scan) in scan 04 was omitted due to a hole in the sample surface. The two line scans 1 and 2 are shorter due to the geometry of the ablation cell. (B) The intensity ratios of $^{55}Mn^{+}/^{57}Fe^{+}$ are plotted for the same line scans as A. The ratios are noisier for the left side than for the right side. All ratios are stable except for scan 12, where ratios slightly increase to the right.

Surprisingly, simulations with a single or a second He gas inlet, respectively, revealed only minor differences in the simulated gas flow pattern. However, a second gas inlet in the other corner drastically decreased purging time of ambient air after opening of the cell for sample replacement. The simulations of the sled positions left (q) and right (p) are nearly symmetric. However, intensity of the signals is more stable and RSDs of the signals are smaller for the left (q) position when compared to the right (p) position (Fig. 2D). This may be due to low transient changes in the gas flow pattern. Such are not considered in a steady state CFD, and could be different between the two sides with only one gas inlet. The residence time of the aerosol inside the transport tube (90 cm) was calculated to be 680 ms, and gas velocity in the slow flow regime is roughly 1 cm s^{-1}. Depending on the position of the ablation, the distance traveled by the aerosol from the ablation spot to the transport tube can be up to 4 cm. On average, this yields a response time of 1–2 s from starting the ablation to detecting signal in the MS.

3.2. Washout

The washout of the ablation cell and the transport of the laser generated aerosol to the ICP are crucial parameters for main and trace element analyses with high spatial resolution, as mentioned above. Hence, it should be as short as possible to avoid mixing of the aerosols from different spots and therefore maintain information from the sampling position. This is optimally achieved with a laminar gas flow between sample surface and ablation window with gas flow vectors pointing towards the gas outlet at all positions [40]. The total volume of the cell seems to be irrelevant as long as the gas flows under the ablation window (ablation site) are favorable for fast washout, as indicated by the modeling. It appears that the washout process of the aerosol involves two processes, here referred to as fast washout and slow washout (Fig. 5). The fast washout is a sharp decrease in signal intensity, 2–3 by orders of magnitude (to signal intensities as low as 0.1–1%) within 1.3–2.6 s after the last laser pulse. The slow washout requires significantly more time (up to 10.4 s) and accounts for the time required for the signal to drop back to background level (Fig. 2D). Arrowsmith and Hughes [17] have explained such long washout with aerosol that escaped the ablation plume entrainment device (the inner cell in their study). As a result, a small quantity of aerosol is dispersed into the outer cell volume and requires more time (more than 14 min in their experiment) to be washed out completely. There is no inner cell in our setup, hence, the slow washout might be due to particles that are thrust away from the outlet upon ablation. These particles end up in a slow gas flow regime, resulting in a longer washout. Dispersion of the aerosol in the transport tube [16,31,40,41] also contributes to this effect, at least to some extent. However, the major contribution to signal dispersion and washout is related to the cell. We determined for our setup a complete washout (signal intensity down to background level), which includes the fast and the short washout time in the order of 4.6–12.4 s. The two extreme positions q-l and p-r (Fig. 2D) feature the longest washout time, as for these configurations ablation takes place in low gas flow areas indicated by the simulations. The difference in washout between these two cell configurations can be explained by two parameters: (A) the high gas flow velocities are pointing towards the gas outlet in the new cell configuration and (B) the total volume of the cell for aerosol expansion is 2.5 times smaller than for the standard configuration discussed in Koch et al. [40].

The washout of the new cell was compared to the washout of the standard cylindrical ablation cell [37] with a washout time of approximately 25 s (Fig. 5). The washout of the new cell was deter-

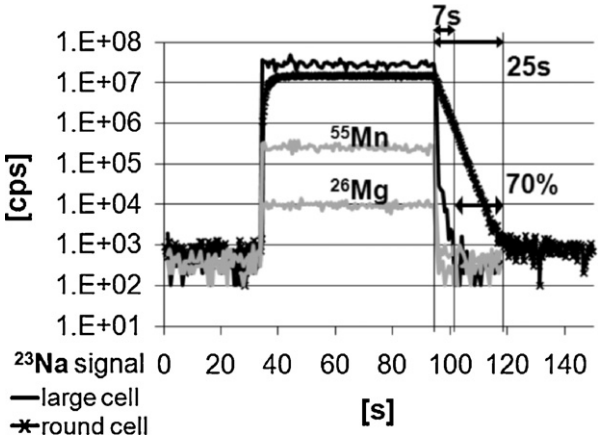

Fig. 5. The comparison of the aerosol washout after 60 s of LA illustrates the different behavior of the two cells for rise and decay of the signal. The washout is 70% faster in the large cell compared to the standard (cylindrical) cell [37]. Two other signals (Mn and Mg) with lower intensities are plotted as examples for fast washout of trace elements in the large cell.

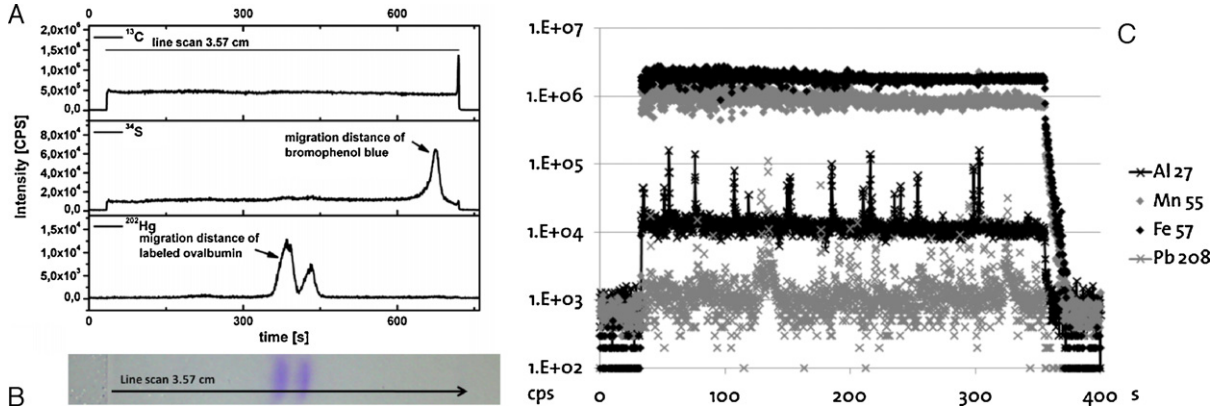

Fig. 6. (A) Signals of a line scan on the gel of $^{13}C^+$, $^{34}S^+$, and $^{202}Hg^+$ containing Hg derivatized ovalbumin is shown, with the beginning of the separation gel set as starting point. The transient signal of $^{13}C^+$ as a matrix element is constant during the line scan. The migration distance of bromophenol blue is indicated by the $^{34}S^+$ signal (ca. 700 s). There are two clearly separated signals visible in the $^{202}Hg^+$ trace, indicating two different species present in the derivatised ovalbumin (signals at 380 and 450 s, respectively). The peak at the end of the $^{13}C^+$ signal comes from short ablation of tape that was used to hold the gel in place. (B) Picture of the Coomassie Blue stained gel for comparison with 1 mm between the two protein bands. (C) Plot of signals of scan 09 on JK-2D. Fe and Mn are homogeneously distributed in the steel standard (but noisier for the left side) while Al (84% RSD) and Pb (256% RSD) are inhomogeneously distributed.

mined to be 87% faster for the first 3 orders of magnitude of signal reduction in comparison to the standard cell.

3.3. Intensities and RSDs

The overall variability in signal intensities (signal height) measured within the cell was 11.5% RSD and showed no indication for reduced transport efficiency in comparison to the standard cell. The signal intensities were 11.8% lower when placing the sample directly in the center in front of the gas outlet (q–m, o–m, p–m). The position of the sled showed no influence. However, the intensities were 1.6% and 10.2% higher for the two other samples at positions l and r (Fig. 2D), respectively. This may be explained by the lower gas flow velocities (between 2 and 3 times lower) in the center. Therefore, the aerosol generated there is transported slower than that generated in a fast flow area. Optimum cell designs need to offer a more uniform flow pattern and thus, aerosol transport at any position within the ablation cell. Constant gas flows in the entire ablation area and all flow vectors pointing towards the outlet would be ideal. They could prevent the creation of vortices that are prone to trap the aerosol, which leads consequently to an increase in washout time in certain regions. However, as shown by the results (Fig. 2), the asymmetric low gas flow has almost no influence on signal intensity (samples l and r), whereas the complete washout is most significantly influenced (Fig. 2D).

The experiments indicate a dependence of the signal on the sled position. When the sled is on the far side from the He inlet, signal intensity is more similar and stability of the signal (RSD) is higher. In that position signal RSDs are lower than 20% in 8 out of 9 experiments. The RSDs become larger for those analyses in areas with faster gas flow, e.g., the center position of the sled (symmetric gas flow) leads to signals with higher RSD values (between 20 and 30% and for one particular measurement higher than 50%) as indicated by the *o-l* analyses (see Fig. 2). During three successive measurements with this set-up, the signal for the first measurement (*o-l-1*) showed a high RSD due to a periodic 'wavy' variation [22,42] described as spectral skew. For the second run within the same ablation scan (*o-l-2*) the spectral skew was smaller and vanished for the third run (*o-l-3*) when the signal showed mainly random variation. This may be due to changes in the expansion properties of the ablation plume, when each of the three scans ablates deeper in the sample, thus the plumes of the three scans spread into different gas flow regimes for each of the scans. Other possible factors can be vibrations of the sample from the xyz-stage, or varying flow pattern in the course of analysis resulting in subtle pressure waves reaching the ICP. The influence of pressure oscillations on the ICP-MS signal have been reported by Hirata [43].

3.4. Imaging

Based on the experiments and optimization process, a second gas inlet was added to the final configuration of the cell. Twelve line scans were performed across the surface for monitoring signal stability and washout in dependence on the sampling position. The following analyses were carried out using two He gas inlets with equal gas flow rate of 0.5 L min^{-1} each, a total of 1.0 L min^{-1} He. This change led to a signal stability in the order of 13–28% RSDs for the left side and 6–18% RSDs for the right side, if the line scan would be split in the middle (Fig. 4). The dimensions of the steel CRM JK-2D are close to the area accessible by the laser through the ablation cell window without moving the sample sled. Scan 01 is close to the sample holder, where irregular gas flows cause some fluctuations in the signal intensity. Furthermore, the signal intensity for Scan 12 is twofold higher than that of Scan 11 and decreases along the line scan, because it is as close as 0.5 mm to the other sample holder (Fig. 4A). This indicates that measurements should not be performed close to the sample holders. As shown in Fig. 4B, the ratios of $^{55}Mn^+/^{57}Fe^+$ are stable along the line scans, except for Scan 12, where this ratio increases. In conformity to the intensities, also the ratios of $^{55}Mn^+/^{57}Fe^+$ are noisier for the left side (average over 12 line scans: 0.50 ± 0.04, RSD: 8.2%) compared to the right side (average over 12 line scans: 0.46 ± 0.01, RSD: 2.4%). A slight difference in the two gas flows might be a source of oscillation, which causes a resonance within the cell. Since this effect was reproducible when the direction of the scan was inverted, the ablation process is not responsible for that. It is possible that a standing wave is created either by the shockwave of the ablation or by unequal division of the carrier gas upstream of the cell by the T-fitting. The reason for this phenomenon is not yet fully understood. The washouts for the scans that are further away from the outlet are considerably longer (Fig. 4A) than for those scans close to the outlet. As indicated by the modeling, a slow gas flow regime at that position may slow down aerosol in a dynamic trap, resulting in slower washout.

Among the elements that were monitored (Table 1) for the analyses of JK-2D, it was found, that Al and Pb are distributed heterogeneously (Fig. 6C) within the sample, in accordance with the findings by Wiltsche and Günther [44].

3.5. Application of the ablation cell

For the ablation of gels, line scans over the entire separation gel length were performed (35.7 mm length). The beginning of the separation gel was defined optically, whereas the final migration distance of bromophenol blue as a marker could be traced by the $^{34}S^+$ intensity. Fig. 6A shows the distribution of mercury within the gel. Comparison of R_f values between the stained gel and LA is in good agreement. Although the samples contained ovalbumin only, two separated signals were observed. As both signals are also observed in the underivatized protein (see Coomassie stained gel, Fig. 6B), it can be concluded, that there is more than one species present in ovalbumin (for example due to phosphorylation or glycosilation), which is consistent with previous studies [39,45]. Two forms of ovalbumin were separated with a chromatographic resolution of $R = 1.1$ (FWHM). As shown in the previous experiments, scanning from left to right in the cell gives a slightly higher RSD (4–5%) for matrix elements, in this case $^{13}C^+$. The washout for $^{13}C^+$ was accomplished within 8 s from 1.4×10^6 cps to 1.8×10^4 cps background. This is longer than for particle transport, which suggests that washout of formed gaseous species of carbon [46] follows different laws than that of aerosol.

4. Conclusion

A large ablation cell capable of holding large objects was designed, built and tested successfully with three different sample types (glass, metal, organic matrix). It is shown that this ablation cell is able to provide high spatial resolution data of main and trace elements as well as hosting of large samples. A fast washout is achieved by restricting the effective volume for the expansion of the laser-generated aerosol at the ablation site with a geometry favoring laminar gas flows.

The source of the spectral skew and noisier half of the signal remains to be investigated. With this large ablation cell, it was possible to mount two electrophoresis gels simultaneously for the acquisition of Hg profiles in a gel. This allowed the detection of the separated protein and the determination of retention factors. The achieved resolution was limited by the resolution of the gel (and the large diameter of the bands), but such a large cell was necessary for hosting these large samples. Using this cell for imaging of the steel standard, we are able to detect small inhomogeneities (Al and Pb hotspots) that are present in the sample.

The major advantages of this cell design are the fast washout and the possibility to place either a number of samples or a large one into the sample holder. This allows fast switching from standards to the sample of interest and reduces the current necessity of cutting samples (drilling cores, sediments, corals, tree rings, etc.). Therefore, this type of ablation cell allows the analysis of a batch of samples without opening of the cell between analyses [47], which is a promising tool for further automation of the technique. The motorization of the inner sledge to move the sample along one single ablation position is currently in progress and will contribute to improve the stability of the signal intensity.

Acknowledgements

The authors would like to dedicate the manuscript to Prof. Dr. Dietze's 75th birthday and would like to thank him for many fruitful discussions on LA-ICP-MS and science in general.

ETH Zurich is acknowledged for funding of the project. Furthermore, the authors would like to thank Roland Mäder (ETH Zurich, machine shop, LAC) for building the ablation cell. The group of Prof. Hilvert at ETH Zurich is kindly acknowledged for the possibility of using the electrophoresis unit. Two anonymous reviewers are acknowledged for very valuable comments which helped improving the manuscript. D.K. would like to acknowledge the Spanish ministry for education for a Ph.D. grant.

References

[1] R.E. Russo, X. Mao, H. Liu, J. Gonzalez, S.S. Mao, Laser ablation in analytical chemistry—a review, Talanta 57 (2002) 425–451.
[2] G. Fontaine, K. Hametner, A. Peretti, D. Günther, Authenticity and provenance studies of copper-bearing andesines using Cu isotope ratios and element analysis by fs-LA-MC-ICPMS and ns-LA-ICPMS, Anal. Bioanal. Chem. 398 (2010) 2915–2928.
[3] A. Plotnikov, C. Vogt, K. Wetzig, An approach to the reconstruction of true concentration profile from transient signal in spatially resolved analysis by means of laser ablation ICP-MS, J. Anal. At. Spectrom. 17 (2002) 1114–1120.
[4] J. Wirth, S. Poletti, B. Aeschlimann, N. Yakandawala, B. Drosse, S. Osorio, T. Tohge, A. Fernie, D. Günther, W. Gruissem, C. Sautter, Rice endosperm iron biofortification by targeted and synergistic action of nicotianamine synthase and ferritin, Plant Biotechnol. J. 7 (2009) 631–644.
[5] D.J. Sinclair, L.P.J. Kinsley, M.T. McCulloch, High resolution analysis of trace elements in corals by laser ablation ICP-MS, Geochim. Cosmochim. Acta 62 (1998) 1889–1901.
[6] A.J. Campbell, M. Humayun, Trace element microanalysis in iron meteorites by laser ablation ICPMS, Anal. Chem. 71 (1999) 939–946.
[7] M. Bi, A.M. Ruiz, I. Gornushkin, B.W. Smith, J.D. Winefordner, Profiling of patterned metal layers by laser ablation inductively coupled plasma mass spectrometry (LA-ICP-MS), Appl. Surf. Sci. 158 (2000) 197–204.
[8] A. Raab, B. Ploselli, C. Munro, J. Thomas-Oates, J. Feldmann, Evaluation of gel electrophoresis conditions for the separation of metal-tagged proteins with subsequent laser ablation ICP-MS detection, Electrophoresis 30 (2009) 303–314.
[9] J.M. Cottle, M.S.A. Horstwood, R.R. Parrish, A new approach to single shot laser ablation analysis and its application to in situ Pb/U geochronology, J. Anal. At. Spectrom. 24 (2009) 1355–1363.
[10] P. Treble, J.M.G. Shelley, J. Chappell, Comparison of high resolution sub-annual records of trace elements in a modern (1911–1992) speleothem with instrumental climate data from southwest Australia, Earth Planet Sci. Lett. 216 (2003) 141–153.
[11] J.S. Becker, M.V. Zoriy, C. Pickhardt, N. Palomero-Gallagher, K. Zilles, Imaging of copper, zinc, and other elements in thin section of human brain samples (hippocampus) by laser ablation inductively coupled plasma mass spectrometry, Anal. Chem. 77 (2005) 3208–3216.
[12] J.D. Woodhead, J. Hellstrom, J.M. Hergt, A. Greig, R. Maas, Isotopic, Elemental imaging of geological materials by laser ablation inductively coupled plasma-mass spectrometry, Geostand. Geoanal. Res. 31 (2007) 331–343.
[13] S.F. Durrant, Laser ablation inductively coupled plasma mass spectrometry: achievements, problems, prospects, J. Anal. At. Spectrom. 14 (1999) 1385–1403.
[14] R. Ma, C.W. McLeod, K. Tomlinson, R.K. Poole, Speciation of protein-bound trace elements by gel electrophoresis and atomic spectrometry, Electrophoresis 25 (2004) 2469–2477.
[15] J.S. Becker, R. Lobinski, J.S. Becker, Metal imaging in non-denaturating 2D electrophoresis gels by laser ablation inductively coupled plasma mass spectrometry (LA-ICP-MS) for the detection of metalloproteins, Metallomics 1 (2009) 312–316.
[16] D. Bleiner, D. Günther, Theoretical description and experimental observation of aerosol transport processes in laser ablation inductively coupled plasma mass spectrometry, J. Anal. At. Spectrom. 16 (2001) 449–456.
[17] P. Arrowsmith, S.K. Hughes, Entrainment and transport of laser ablated plumes for subsequent elemental analysis, Appl. Spectrosc. 42 (1988) 1231–1239.
[18] C.C. Garcia, H. Lindner, K. Niemax, Transport efficiency in femtosecond laser ablation inductively coupled plasma mass spectrometry applying ablation cells with short and long washout times, Spectrochim. Acta B 62 (2007) 13–19.
[19] D. Autrique, A. Bogaerts, H. Lindner, C.C. Garcia, K. Niemax, Design analysis of a laser ablation cell for inductively coupled plasma mass spectrometry by numerical simulation, Spectrochim. Acta B 63 (2008) 257–270.
[20] J. Feldmann, A. Kindness, P. Ek, Laser ablation of soft tissue using a cryogenically cooled ablation cell, J. Anal. At. Spectrom. 17 (2002) 813–818.
[21] D. Asogan, B.L. Sharp, C.J.P. O'Connor, D.A. Green, R.W. Hutchinson, An open, non-contact cell for laser ablation-inductively coupled plasma-mass spectrometry, J. Anal. At. Spectrom. 24 (2009) 917–923.
[22] W. Müller, M. Shelley, P. Miller, S. Broude, Initial performance metrics of a new custom-designed ArF excimer LA-ICPMS system coupled to a two-volume laser-ablation cell, J. Anal. At. Spectrom. 24 (2009) 209–214.
[23] E.L. Gurevich, R. Hergenröder, A simple laser ICP-MS ablation cell with wash-out time less than 100 ms, J. Anal. At. Spectrom. 22 (2007) 1043–1050.
[24] Y. Liu, Z. Hu, H. Yuan, S. Hu, H. Cheng, Volume-optional and low-memory (VOLM) chamber for laser ablation-ICP-MS: application to fiber analyses, J. Anal. At. Spectrom. 22 (2007) 582–585.
[25] J. Pisonero, D. Fliegel, D. Günther, High efficiency aerosol dispersion cell for laser ablation-ICP-MS, J. Anal. At. Spectrom. 21 (2006) 922–931.
[26] D. Bleiner, H. Altorfer, A novel gas inlet system for improved aerosol entrainment in laser ablation inductively coupled plasma mass spectrometry, J. Anal. At. Spectrom. 20 (2005) 754–756.

[27] D. Monticelli, E.L. Gurevich, R. Hergenröder, Design and performances of a cyclonic flux cell for laser ablation, J. Anal. At. Spectrom. 24 (2009) 328–335.
[28] M. Tanner, D. Günther, A new ICP–TOFMS. Measurement and readout of mass spectra with 30 μs time resolution, applied to in-torch LA-ICP-MS, Anal. Bioanal. Chem. 391 (2008) 1211–1220.
[29] Z. Hu, Y. Liu, S. Gao, S. Hu, R. Dietiker, D. Günther, A local aerosol extraction strategy for the determination of the aerosol composition in laser ablation inductively coupled plasma mass spectrometry, J. Anal. At. Spectrom. 23 (2008) 1192–1203.
[30] D. Bleiner, A. Bogaerts, Computer simulations of sample chambers for laser ablation-inductively coupled plasma spectrometry, Spectrochim. Acta B 62 (2007) 155–168.
[31] H. Lindner, D. Autrique, C.C. Garcia, K. Niemax, A. Bogaerts, Optimized transport setup for high repetition rate pulse-separated analysis in laser ablation-inductively coupled plasma mass spectrometry, Anal. Chem. 81 (2009) 4241–4248.
[32] T. Jilbert, G.-J. Reichart, B. Aeschlimann, D. Günther, W. Boer, G. de Lange, Climate-controlled multidecadal variability in North African dust transport to the Mediterranean, Geology 38 (2010) 19–22.
[33] M.S. Roberts, P.L. Smart, C.J. Hawkesworth, W.T. Perkins, N.J.G. Pearce, Trace element variations in coeval Holocene speleothems from GB Cave, southwest England, Holocene 9 (1999) 707–713.
[34] D. Pozebon, V.L. Dressler, M. Foster Mesko, A. Matusch, J.S. Becker, Bioimaging of metals in thin mouse brain section by laser ablation inductively coupled plasma mass spectrometry: novel online quantification strategy using aqueous standards, J. Anal. At. Spectrom. 25 (2010) 1739–1744.
[35] M. Sanborn, K. Telmer, The spatial resolution of LA-ICP-MS line scans across heterogeneous materials such as fish otoliths and zoned minerals, J. Anal. At. Spectrom. 18 (2003) 1231–1237.
[36] M. Senoner, T. Wirth, W.E.S. Unger, Imaging surface analysis: lateral resolution and its relation to contrast and noise, J. Anal. At. Spectrom. 25 (2010) 1440.
[37] B. Hattendorf, Ion molecule reactions for the suppression of spectral interferences in elemental analysis by inductively coupled plasma mass spectrometry, ETH Zurich Dissertation DISS, ETH NO. 14926, 2002.
[38] ANSYS® Academic Research, Release 12.1, CFX, ANSYS, Inc., 2009.
[39] D.J. Kutscher, M.E. del Castillo Busto, N. Zinn, A. Sanz-Medel, J. Bettmer, Protein labelling with mercury tags: fundamental studies on ovalbumin derivatised with p-hydroxymercuribenzoic acid (pHMB), J. Anal. At. Spectrom. 23 (2008) 1359–1364.
[40] J. Koch, M. Wälle, R. Dietiker, D. Günther, Analysis of laser-produced aerosols by inductively coupled plasma mass spectrometry: transport phenomena and elemental fractionation, Anal. Chem. 80 (2008) 915–921.
[41] R. Kovacs, D. Günther, Influence of transport tube materials on signal response and drift in laser ablation-inductively coupled plasma-mass spectrometry, J. Anal. At. Spectrom. 23 (2008) 1247–1252.
[42] T. Pettke, C. Heinrich, A. Ciocan, D. Günther, Quadrupole mass spectrometry and optical emission spectroscopy: detection capabilities and representative sampling of short transient signals from laser-ablation, J. Anal. At. Spectrom. 15 (2000) 1149–1155.
[43] T. Hirata, Development of an on-line low gas pressure cell for laser ablation-ICP-mass spectrometry, Anal. Sci. 23 (2007) 1195–1201.
[44] H. Wiltsche, D. Günther, Capabilities of femtosecond laser ablation ICPMS for the major, minor and trace element analysis of high alloyed steels and super alloys, Anal. Bioanal. Chem. (2011), doi:10.1007/s00216-010-4605-8.
[45] J.A. Saba, X. Shen, J.C. Jamieson, H. Perreault, Investigation of different combinations of derivatization, separation methods and electrospray ionization mass spectrometry for standard oligosaccharides and glycans from ovalbumin, J. Mass Spectrom. 36 (2001) 563–574.
[46] J.-L. Todolí, J.-M. Mermet, Study of polymer ablation products obtained by ultraviolet laser ablation-inductively coupled plasma atomic emission spectrometry, Spectrochim. Acta B 53 (1998) 1645–1656.
[47] F. Vanhaecke, M. Resano, J. Koch, K. McIntosh, D. Günther, Femtosecond laser ablation-ICP-mass spectrometry analysis of a heavy metallic matrix: determination of platinum group metals and gold in lead fire-assay buttons as a case study, J. Anal. At. Spectrom. 25 (2010) 1259–1267.